Mechanisms of Flow-induced Signal Loss in MR Angiography[1]

Steven N. Urchuk, MSc • Donald B. Plewes, PhD

Mechanisms of signal loss in magnetic resonance angiography were studied with a stenotic flow phantom. The results indicate that while signal loss induced by mean fluid motions is localized about the stenosis, the fluctuating component of fluid motion induces signal loss over a much larger region, primarily distal to the stenosis. For both motion components, use of gradient moment nulling (GMN) above first order was found to be an ineffective means of reducing signal loss. In contrast, shortened gradient durations were found to reduce signal loss substantially. However, though a zeroth-order gradient is generally of the shortest duration, use of a slightly longer, first-order gradient was found to be the most robust means of reducing signal loss.

Index terms: Flow artifact • Gradient waveforms • Model, mathematical • Phantoms • Physics • Pulse sequences • Vascular studies, 9•.1214

JMRI 1992; 2:453–462

Abbreviation: GMN = gradient moment nulling.

MAGNETIC RESONANCE (MR) ANGIOGRAPHY is a noninvasive vascular imaging technique that has shown considerable promise (1–6). At present, most approaches are variants of either time-of-flight (1–5) or phase-contrast methods (6). These approaches rely on acquisition methods that produce a strong signal from flowing blood relative to stationary tissues. Unfortunately, current techniques have proved sensitive to signal loss induced by flow disturbances. Because these disturbances are often associated with stenoses and regions of complex vascular anatomy (7,8), the potential for exaggeration or mimicking of the appearance of vascular disease by signal loss is an important clinical problem.

Flow disturbances (characterized by the presence of a fluctuating motion superimposed on a primary, or mean, motion) induce signal loss through the mechanism of spin dephasing (9–11). To reduce these artifacts, most MR angiography techniques use some combination of "flow compensation" strategies (eg, gradient moment nulling [GMN] [2–5,12–14], shortened gradient durations and reduced TEs [1–5], and/or small voxels [3–6]). Although these strategies have proved effective for relatively quiescent flow, reduction of signal loss due to disturbed flow has proved to be more difficult (1–6). In part, this situation is a consequence of the difficulties inherent in characterizing signal loss induced by disturbed flow.

Models of flow-induced signal loss have generally been based on statistical descriptions of the fluctuating component of fluid velocity. Development of these models has proceeded along a number of alternate lines, with use of, for example, the probability distribution governing fluid motion (15), the statistical moments of the fluid velocity distribution (16–20), the motion power spectrum (21), or eddy diffusivity (22,23). However, experimental confirmation of these models has primarily been limited to relatively simple flow systems, such as flow through straight pipes (15–18,20). In these systems, the mean velocity distribution can be approximated as spatially invariant at sufficiently high flow rates. Although this assumption is a useful simplification, it does not extend to flow through stenoses, where generally the mean and fluc-

[1] From the Sunnybrook Health Science Centre, Department of Medical Biophysics, University of Toronto, 2075 Bayview Ave, Toronto, Ont, Canada M4N 3M5. From the 1991 SMRI annual meeting. Received February 7, 1992; accepted March 13. Supported in part by the Medical Research Council of Canada, the National Cancer Institute of Canada, Creare.x, Inc, and GE Medical Systems. **Address reprint requests to** D.B.P.

tuating components of flow velocity vary in both space and time. Basic studies of these more complex geometries have been performed only to a limited extent (23). It is the purpose of the present study to address this problem by considering signal loss mechanisms, both experimentally and theoretically, in a more realistic stenotic flow phantom. Specifically, the relative contributions of mean and fluctuating fluid motions to signal loss will be considered. Finally, the ability of GMN and shortened gradient durations to reduce flow-induced signal loss will be evaluated.

In the following section, theoretical aspects of signal loss will be developed and used to derive numerical estimates of signal loss in our model system, for comparison with experimental observations.

• THEORY

A description of flow-induced signal loss can be developed in terms of the applied magnetic field gradients and flow velocity. Consider the time evolution of the transverse magnetization $m(\mathbf{r}, t)$ in a Lagrangian frame of reference. In this frame, the motion of individual fluid particles (ie, spins) is followed over time t. The positions (or trajectories) $\mathbf{r}$ of the particles are determined by their instantaneous velocities $\mathbf{v}(\mathbf{r}_0, t)$ and initial positions $\mathbf{r}_0$:

$$\mathbf{r}(\mathbf{r}_0, t) = \mathbf{r}_0 + \int_0^t \mathbf{v}(\mathbf{r}_0, t')dt'. \quad (1)$$

In disturbed flow, $\mathbf{v}(\mathbf{r}_0, t)$ is composed of mean, $\langle\mathbf{v}(\mathbf{r}_0, t)\rangle$, and fluctuating, $\mathbf{v}'(\mathbf{r}_0, t)$, components (24, p 7):

$$\mathbf{v}(\mathbf{r}_0, t) = \langle\mathbf{v}(\mathbf{r}_0, t)\rangle + \mathbf{v}'(\mathbf{r}_0, t). \quad (2)$$

In general, while the mean velocity component is a smooth function of space and time, the fluctuating component varies randomly in space and time (24, p 125). Phase changes induced by these motion components can be described by considering the Bloch equation governing $m(\mathbf{r}, t)$:

$$\frac{d}{dt} m(\mathbf{r}, t) = [i\gamma\mathbf{G}(t) \cdot \mathbf{r}(\mathbf{r}_0, t)]m(\mathbf{r}, t), \quad (3)$$

where γ is the gyromagnetic ratio and $\mathbf{G}(t)$ is the applied magnetic field gradient. Combining Equations (1)–(3) and solving for $m(\mathbf{r}, t)$ we have

$$m(\mathbf{r}, t) = m(\mathbf{r}, 0) \exp [i\langle\varphi(\mathbf{r}, t)\rangle + i\varphi'(\mathbf{r}, t)], \quad (4)$$

where $\langle\varphi(\mathbf{r}, t)\rangle$ and $\varphi'(\mathbf{r}, t)$ are the mean and fluctuating components of the magnetization phase:

$$\langle\varphi(\mathbf{r}, t)\rangle = \gamma \int_0^t \mathbf{G}(t') \cdot [\mathbf{r}_0 + \int_0^{t'} \langle\mathbf{v}(\mathbf{r}_0, t'')\rangle dt'']dt', \quad (5)$$

$$\varphi'(\mathbf{r}, t) = \gamma \int_0^t \mathbf{G}(t') \cdot \int_0^{t'} \mathbf{v}'(\mathbf{r}_0, t'')dt''dt'. \quad (6)$$

As indicated by this result, the distribution of the mean and fluctuating phase components will reflect the distribution of the two velocity components. Consequently, the character of the mean and fluctuating components of signal loss can differ considerably. However, since both motion components influence signal loss through spin dephasing, the relative contribution of each motion component to signal loss cannot be determined solely by experimental means. Our approach to determining their relative contributions is based on comparisons of experimental observations of signal loss with numerical simulations of signal loss induced by only the mean component of motion. In the following section, we will outline details of our experimental protocol for quantifying flow-induced signal loss.

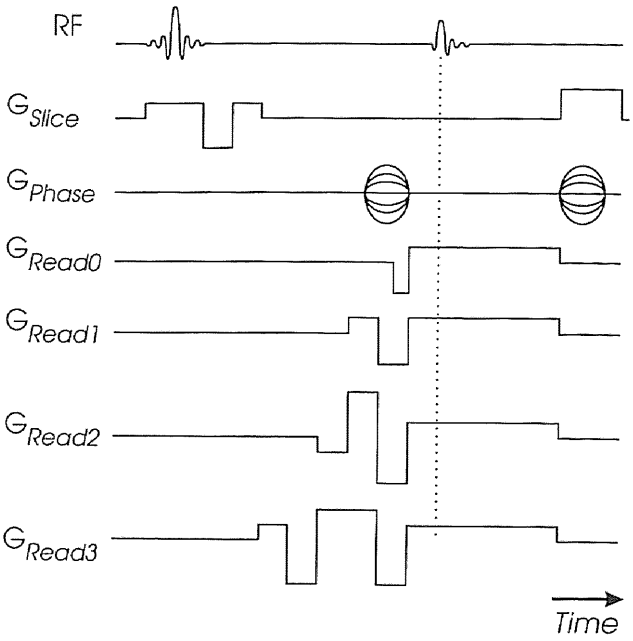

Figure 1. Pulse sequence diagram. The gradients G_{Read0} through G_{Read3} were incorporated to allow GMN up to third order. An echo asymmetry of 25% is illustrated.

• MATERIALS AND METHODS

Experimental

All experiments were performed with a clinical 1.5-T MR imager (Signa; GE Medical Systems, Milwaukee) equipped with a self-shielded gradient system capable of 10-mT/m peak amplitudes and rise times of 600 μsec. In Figure 1, a timing diagram of the modified time-of-flight MR angiography pulse sequence used in this study is shown. The sequence incorporated GMN of a variable order in the readout direction and first-order GMN in the section-select direction. GMN was not used in the phase-encoding direction. To control the duration of the readout-gradient dephasing lobes, an echo of variable asymmetry was incorporated into the sequence. This allowed the formation of echoes with up to 40% asymmetry (ie, echoes shifted by 40% of the data sampling time toward the beginning of data acquisition). For a 200-mm field of view and a 32-kHz sampling bandwidth, minimum durations of readout-gradient dephasing lobes were 2.3, 5.1, 7.1, and 9.9 msec, for zeroth- through third-order gradients, respectively.

A free-jet flow phantom that exhibits many features of stenotic flow, including convective acceleration and flow disturbances, was used in this study. An aqueous

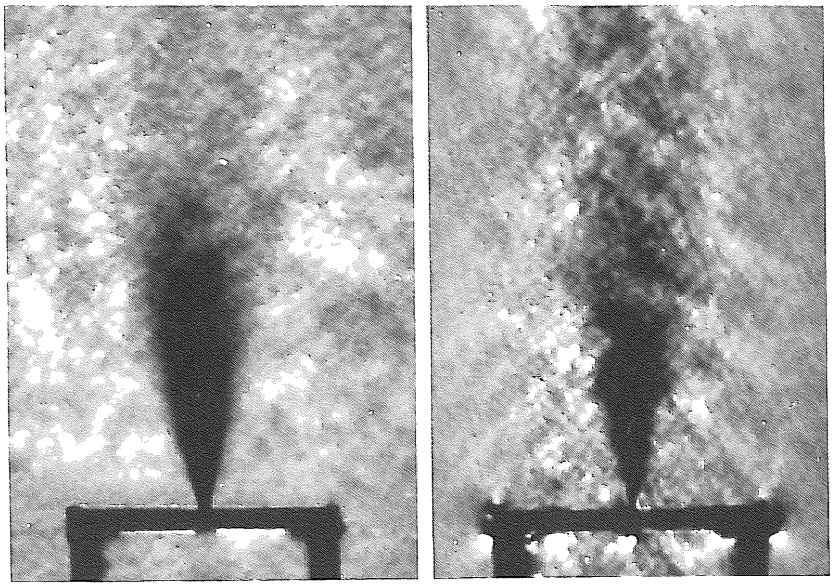

a. b.

Figure 2. Experimental gradient-echo images of the free-jet phantom, with the readout gradient aligned parallel (**a**) and perpendicular (**b**) to the main flow direction. The images were acquired with a symmetric echo and first-order GMN on the section-select and readout gradients. Both images were acquired with a TE of 23 msec, TR of 50 msec, and flip angle of 10°. The in-plane resolution was 0.8 mm, and the section thickness was 10 mm.

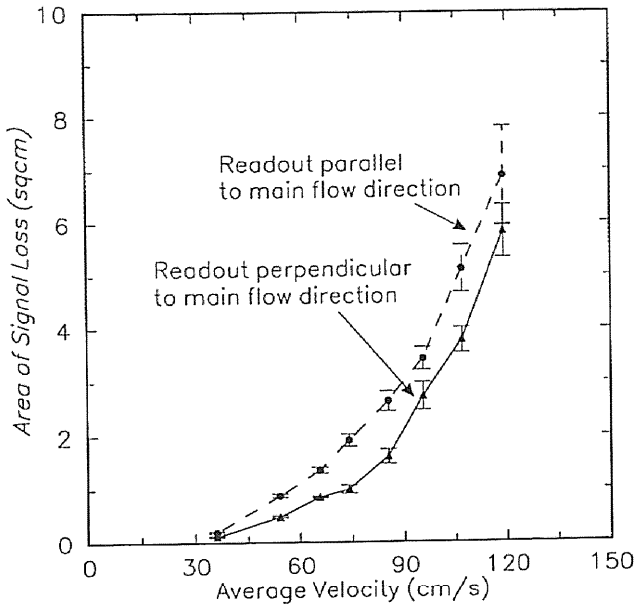

Figure 3. Area of signal loss plotted versus the average velocity through the flow constriction. Image acquisition parameters were the same as those indicated in the legend to Figure 2.

solution of 1.0-mmol/L copper sulfate was used to make the T1 and T2 of the fluid within the phantom on the order of those of blood (25). The phantom was composed of a flat plate (5 mm thick) containing a thin rectangular slot (1.6 × 30 mm) from which steady flow issued into a large cylindric (139 × 600 mm) fluid-filled reservoir. Because of the symmetric nature of this design, the mean velocity parallel to the long axis of the slot was negligible near the slot midpoint. By acquiring images with the section-select direction parallel to the long axis of the slot and the section center positioned at the slot midpoint, we could use the two-dimensional flow field of the phantom to simplify our experimental protocol. As we will demonstrate, under these experimental conditions the motion in the section-select direction produced negligible signal loss.

Typical images of the flow phantom, obtained with the readout gradients oriented parallel and perpendicular to the main flow direction, are shown in Figure 2. For both images, the average velocity through the flow constriction was 120 cm/sec, a value characteristic of velocities that can develop near stenotic lesions in major blood vessels (7). At this flow rate, a large region of disturbed flow exists distal to the constriction. On the experimental images, this is indicated by a region of signal loss and ghosting. Notably, the overall size of the signal loss region remains relatively unaffected by the change in readout-gradient orientation.

To quantify the signal loss observed experimentally, the area of the region attenuated to at least 50% of the signal level outside the region affected by the jet was measured over a range of flow rates. Four images were acquired for each flow rate, and the average of the four signal loss areas was then used to characterize the signal loss for that flow rate. The standard deviation of each set of four images was used to characterize measurement reproducibility. At each flow rate, two sets of experiments were conducted, with the readout gradient either parallel or perpendicular to the main flow direction. As shown in Figure 3, for both sets of data, there is a threshold for the onset of signal loss, followed by a rapid increase in the size of the signal loss region as a function of flow rate. Notably, the signal loss areas measured for the two gradient orientations are similar over the range of flow rates tested, suggesting that the fluid motions inducing the signal loss have some degree of isotropy. Since the mean flow field is primarily unidirectional, this result is consistent with the conclusion that the predominant source of signal loss is the fluctuating com-

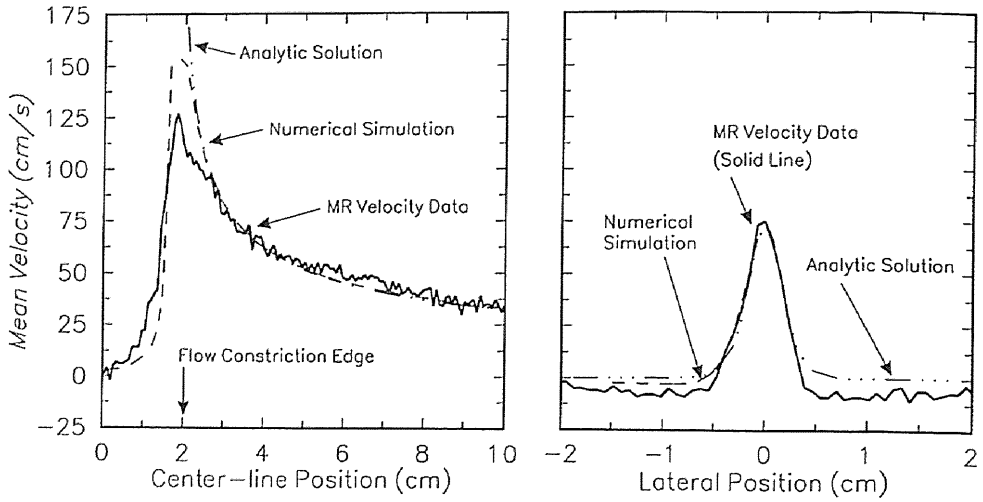

Figure 4. Center-line (left graph) and lateral (right graph) profiles of the mean velocity parallel to the main flow direction. The average velocity through the flow constriction was fixed at 120 cm/sec.

ponent of the fluid motion. However, some component of the signal loss is attributable to phase shifts induced by the mean flow. To demonstrate the importance of this latter phenomenon, a numerical simulation of the signal loss induced by the mean flow was undertaken.

Numerical Simulations

The role of the mean flow in the production of signal loss was demonstrated through numerical simulation. Simulated images of signal loss induced by the mean flow were compared with experimentally obtained images, which reflect signal loss due to both mean and fluctuating motions. This allowed the relative contribution of each type of motion to be determined. Production of a mean-flow signal loss image consisted of four steps: (*a*) simulation of the mean flow field within the phantom, (*b*) calculation of the mean spin trajectories, (*c*) evaluation of the absolute phase shifts induced by spin motion, and (*d*) calculation of the net signal attenuation for a two-dimensional grid of simulated image voxels. Because the mean velocity was zero perpendicular to the image plane, only in-plane flow effects were considered. Further simplification was achieved by assuming that misregistration effects associated with phase encoding were negligible. Thus, only the phase shifts induced by motion during the application of the readout-gradient dephasing lobes required consideration.

Mean Velocity Simulation

A computational fluid dynamics software package (Fluent; Creare.x, Hanover, NH) was used to simulate the mean velocity field $\langle \mathbf{U}(\mathbf{R}) \rangle$, as a function of position $\mathbf{R}$, within the phantom. The program uses a fine grid of computational cells to evaluate the momentum balance within the fluid numerically. Closure of the discrete set of nonlinear differential equations generated in this manner was accomplished through the use of the k-ϵ turbulence model (24, pp 128–130). To ensure an accurate evaluation of these equations, grid points were finely spaced (~ 0.1 mm) near walls and other sites of large velocity gradients. Where velocity gradients were small, a larger grid spacing (~ 1.0 mm) was used for computational efficiency. After simulation, lookup tables for $\langle \mathbf{U}(\mathbf{R}) \rangle$ were formed with two-dimensional bicubic-spline interpolation (26, pp 109–110).

To confirm the accuracy of the simulation, the mean velocity component parallel to the main flow direction was compared with a measurement of the velocity obtained by means of a velocity-sensitive MR pulse sequence (ie, the pulse sequence shown in Fig 1). Two phase images, with readout gradients nulled to the zeroth and first order, were subtracted to form a velocity map. Scaling of this image was based on the sensitivity of the zeroth-order readout gradient to first-order motions (ie, the first moment about TE of the readout-gradient dephasing lobes). To keep the time over which velocity encoding occurs short, and to minimize phase shifts from higher-order motions, data acquisition was performed with an echo with 40% asymmetry. This procedure produced a meaningful phase image over most of the phantom, since the magnitude image was relatively free of flow-induced signal loss. In Figure 4, profiles of the simulated and experimental MR velocity data are presented. The analytic solution for the velocity field of a two-dimensional free jet (27), which is valid for points distal to the flow constriction and near the axis of the jet, is also plotted in Figure 4. An average flow rate of 120 cm/sec was used for this comparison, which is on the order of the highest flow rates considered. Only near the flow constriction do the profiles differ, with MR data underestimating the velocity predicted by the analytic and simulated data. This underestimate can be explained by phase cancellation, due to partial-volume effects and large velocity gradients.

Signal Loss Calculation

Signal loss induced by the mean flow can be estimated by evaluating the mean phase distribution $\langle \varphi(\mathbf{r}, TE) \rangle$ at time TE. Rewriting Equation (6), we have

$$\langle \varphi(\mathbf{r}, TE) \rangle = \gamma \int_0^{TE} \mathbf{G}(t') \cdot \langle \mathbf{r}(\mathbf{r}_0, t') \rangle dt', \qquad (7)$$

where the applied field gradient $\mathbf{G}(t)$ and the mean spin trajectory $\langle \mathbf{r}(\mathbf{r}_0, t) \rangle$ are specified by the parame-

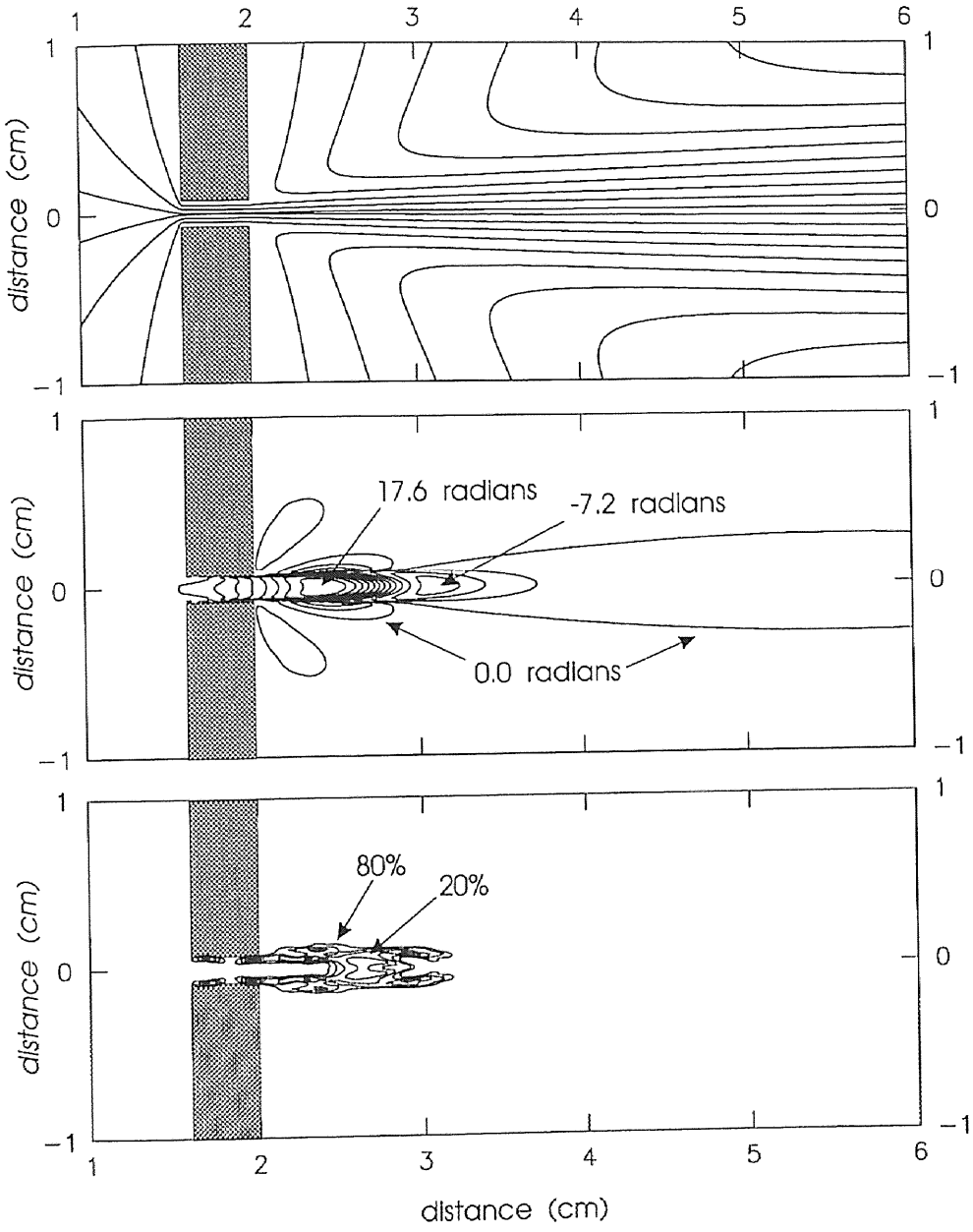

Figure 5. (*Top*) Streamlines of the flow field shown in Figure 3. (*Middle*) The mean phase distribution at TE induced by a readout gradient nulled to first order and oriented in the main flow direction. (*Bottom*) Contour plot of the signal loss induced by the phase distribution shown in the middle plot. In the middle plot, phase contours are separated by 2-radian intervals, while in the bottom plot, signal loss contours are separated by intervals of 20% of the unattenuated signal level in the simulated image.

ters of the imaging sequence and the mean velocity distribution within the fluid, respectively. The mean spin trajectories were determined by numerically integrating the mean spin velocity $\langle \mathbf{v}(\mathbf{r}_0, t) \rangle$ over time:

$$\langle \mathbf{r}(\mathbf{r}_0, t) \rangle = \mathbf{r}_0 + \int_0^t \langle \mathbf{v}(\mathbf{r}_0, t') \rangle dt,$$

$$\langle \mathbf{v}(\mathbf{r}_0, t) \rangle = \langle \mathbf{U}(\mathbf{R}) \rangle, \quad \text{when} \quad \langle \mathbf{r}(\mathbf{r}_0, t) \rangle = \mathbf{R}. \qquad (8)$$

A difficulty with the direct application of this method is that the spatial distribution of spins obtained at time TE will generally be nonuniform if the integration starts from a uniform grid of initial positions. Since it is desirable to have a spatially uniform grid of spin positions at time TE, the spin trajectories were evaluated backward in time, starting from their positions at TE. Fourth-order Runge-Kutta integration was used for the evaluation (26, pp 569–573). To aid in the visualization of the mean trajectories, a streamline plot of the mean flow field simulated in the previous section is presented in Figure 5 (top plot).

After evaluation of the mean trajectories, numerical integration (26, pp 112–123) of Equation (7) was used to compute the spatial distribution of phase at TE. To ensure adequate data sampling for the signal loss calculation, spacing of the phase samples was adjusted to provide an 8 × 8 subgrid of data points within each image voxel. In Figure 5, a contour plot (middle plot) of the phase distribution induced by the flow field described above is shown. A first-order readout gradient, oriented parallel to the main flow direction, was assumed for this example. Notably, regions in which there are appreciable spatial gradients in the phase distribution (ie, phase shifts $> \pi$ radians over a voxel, or $\sim \pi$ radians/mm) are localized about

the flow constriction, indicating that signal loss will be localized about this region.

To quantify signal loss induced by the mean flow, a simulated signal loss image $I(\mathbf{r})$ was formed by convolving $\langle m(\mathbf{r}, TE)\rangle$ with the point spread function $PSF(\mathbf{r})$ of the imaging sequence simulated:

$$I(\mathbf{r}) = \langle m(\mathbf{r}, TE)\rangle * PSF(\mathbf{r}). \quad (9)$$

Here the symbol * is used to denote convolution in the spatial domain. To a first approximation, the point spread function of the imaging sequence may be written (28) as

$$PSF(\mathbf{r}) = \text{sinc}\left(\frac{x}{\Delta x}\right)\text{sinc}\left(\frac{y}{\Delta y}\right), \quad (10)$$

where Δx and Δy are the Nyquist limited spatial resolutions in the frequency-encoding (x) and phase-encoding (y) directions;

$$\text{sinc}(z) = \frac{\sin(\pi z)}{\pi z}. \quad (11)$$

The convolution expressed in Equation (9) is equivalent to a low-pass filtering of $\langle m(\mathbf{r}, TE)\rangle$ by a rectangular filter of bandwidth $2\pi/\Delta x$ in the frequency-encoding direction and $2\pi/\Delta y$ in the phase-encoding direction. To conform with experimental data processing, a further filtration of the image spatial frequencies $\mathbf{k} = (k_x, k_y)$ was performed with a radially symmetric Fermi filter $F(\mathbf{k})$ of the form

$$F(\mathbf{k}) = \frac{1}{1 + \exp\left(\frac{|\mathbf{k}| - \mathbf{k}_0}{\alpha}\right)}, \quad (12)$$

with $\mathbf{k}_0 = \pi/\Delta x = \pi/\Delta y$ and $\alpha = 2\pi/N\Delta x$, where N is the number of image pixels in the frequency- or pulse-encoding direction. These filter parameters produced a radially symmetric point spread function similar in cross section to the sinc point spread function but with side lobes that decrease more rapidly in amplitude. Image blurring related to second- and higher-order phase variations during data sampling was ignored (29), as was blurring associated with T2 signal modulations (28). A sample contour plot of mean-flow signal loss is shown in Figure 5 (bottom), corresponding to the phase distribution in Figure 5 (middle). As expected, signal loss is localized about the flow constriction.

• RESULTS

In the previous sections, a method for differentiating signal loss induced by mean and fluctuating fluid motions was developed. This method will be used to characterize the ability of GMN and shortened gradient durations to reduce signal loss induced by flow within the free-jet phantom.

GMN

GMN is a flow compensation strategy that attempts to reduce signal loss by nulling the sensitivity of a gradient to several, usually low-order motions at TE. To assess the utility of this approach, the free-jet phantom was imaged with readout gradients nulled to the zeroth, first, second, and third order. Images were acquired with a symmetric echo and first-order GMN on the section-select gradient. In Figure 6a–6d, experimental images obtained at an average flow rate of 120 cm/sec are shown. For comparison, the corresponding simulated mean-flow signal loss images are presented in Figure 6e–6h. The experimental images were normalized to the signal intensity of an unattenuated region; hence, they represent a map of the signal fraction attenuated by flow effects. Through this normalization, the experimental and simulated images are directly comparable. Clearly, the area of signal loss measured experimentally is much larger than the area predicted by the mean flow alone, as suggested by Figure 2. Only near the flow constriction, and with the largest gradients in the mean velocity distribution, is signal loss induced by the mean flow substantial.

To illustrate the effect of flow rate on this result, the experimental and simulated mean-flow signal loss areas are shown in Figure 7, for flow rates ranging from 0 to 120 cm/sec. Over this range of flow rates, the experimentally observed signal loss areas are at least one order of magnitude larger than the simulated signal loss areas, for all GMN orders considered. Hence, the area of signal loss observed experimentally approximates the area of signal loss induced by velocity fluctuations alone.

Further insight into the mechanisms of flow-induced signal loss can be obtained by considering the relative performance of the various GMN strategies. As demonstrated by Figures 6 and 7, use of second- or third-order GMN tends to increase the area of signal loss observed at a given flow rate. Furthermore, use of zeroth-order GMN produces a larger area of signal loss than the first-order GMN, which was found to produce the smallest area of signal loss. With the exception of zeroth-order GMN, these observations are valid for both the mean and fluctuating components of signal loss. In the case of zeroth-order GMN, the rate at which the experimentally observed signal loss increases is greater than that for the mean flow.

Many features of these results are explained by the motion sensitivity of the gradients. For motions of order n, the sensitivity $\Gamma_k(n)$ of a gradient nulled to kth-order $G_k(t)$ is given (12) by

$$\Gamma_k(n) = \frac{\gamma}{n!}\int_0^{TE} G_k(t')(t' - TE)^n dt'. \quad (13)$$

Although $\Gamma_k(n)$ is a measure of gradient sensitivity, it is difficult to interpret per se because the absolute magnitude of the motion orders present in the flow is generally unknown. For this reason, we will consider the "relative" gradient sensitivity $\Gamma_{k0}(n)$:

$$\Gamma_{k0}(n) = \frac{\Gamma_k(n)}{\Gamma_0(n)} \quad \text{for} \quad n \geq 1. \quad (14)$$

Use of this quantity facilitates interpretation of relative changes in gradient sensitivity due to GMN, without having to know the motion orders present in the flow. In Figure 8, the relative sensitivities of the zeroth- through third-order gradients are plotted as a

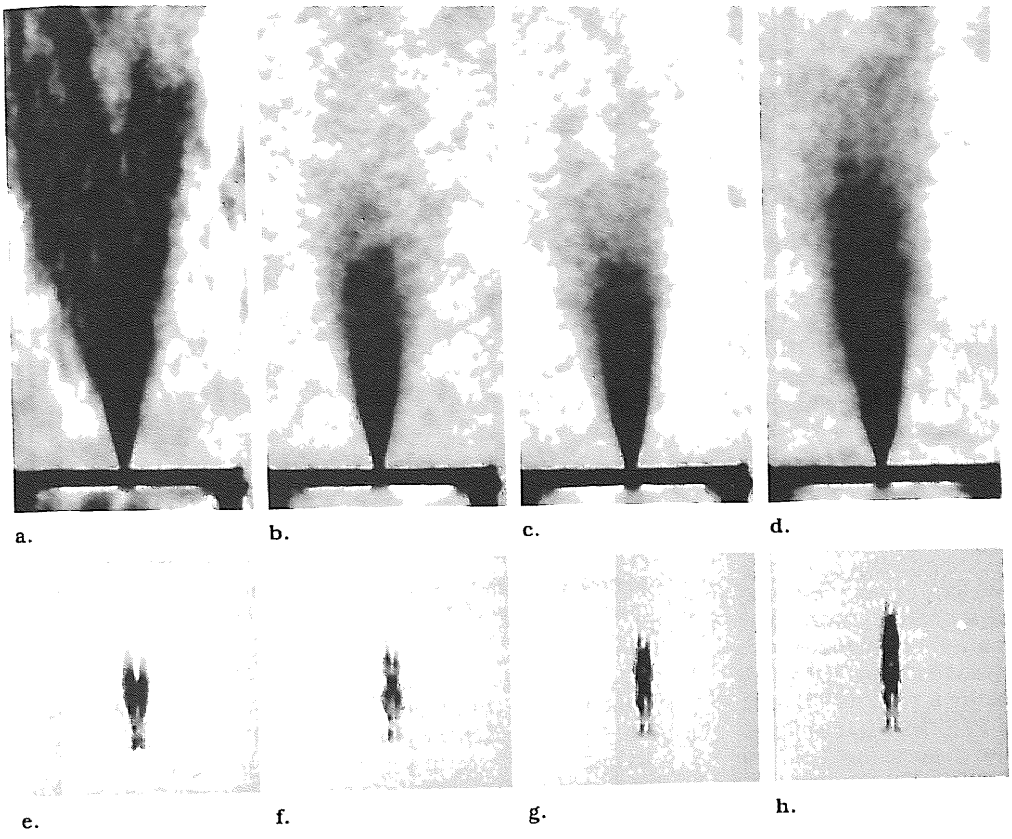

Figure 6. **(a–d)** Experimental gradient-echo images acquired with readout gradients nulled to **(a)** zeroth, **(b)** first, **(c)** second, and **(d)** third order. **(e–h)** Simulated mean-flow signal loss images, corresponding to the four experimental images **(a–d)**, that is, readout gradients moment nulled to **(e)** zeroth, **(f)** first, **(g)** second, and **(h)** third order. Alignment of the readout gradient was parallel to the main flow direction, and the flow rate was fixed at an average value of 120 cm/sec. All other imaging parameters were the same as those indicated in the legend to Figure 2.

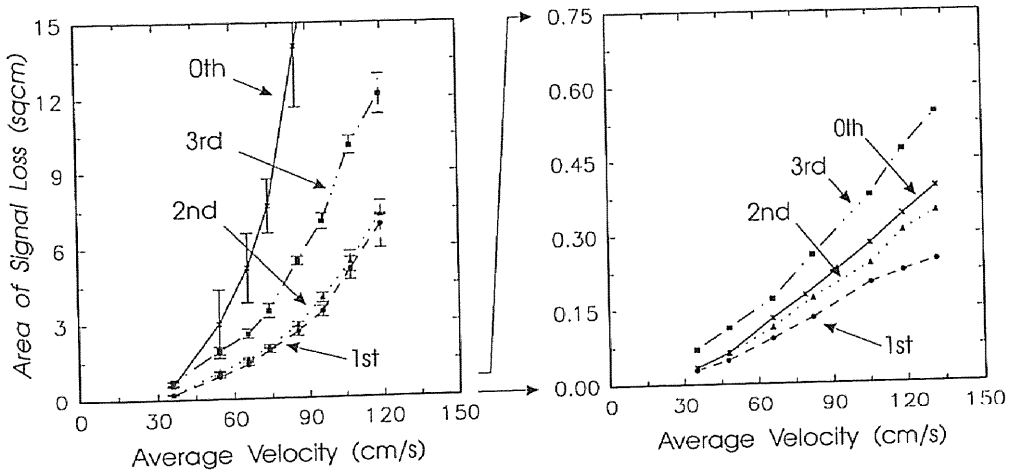

Figure 7. Experimental (left graph) and simulated mean-flow (right graph) signal loss areas plotted versus the average velocity through the flow constriction. Each curve represents data obtained for a given order of GMN (indicated with arrows).

function of motion order. Note that the sensitivity curves are shown only where $\Gamma_{k0}(n)$ is nonzero (ie, for $n \geq k + 1$). Above this threshold, the motion sensitivity of the first- through third-order gradients increases sharply, with the most rapid increase in sensitivity occurring for the higher-order gradients. This is primarily a result of increased gradient durations associated with higher-order GMN. Thus, the failure of higher-order GMN is the result of an elevated gradient sensitivity to motion orders above those nulled. Since regions of disturbed flow typically contain a range of higher-order motions, GMN above first order is likely to be an ineffective means of reducing signal loss in these areas. The failure of zeroth-order GMN to reduce signal loss is a special case. As illustrated in Figure 8, the sensitivity of the zeroth-order gradient is less than (or equal to) the sensitivity of the first-order gradient for all but first-order motions (ie, velocity), to which the sensitivity of the first-order gradient is nulled. Consequently, the nonzero sensitivity of the zeroth-order gradient to first-order motions is sufficiently high to offset its low sensitivity to higher orders of motion.

Though useful for assessing the effectiveness of different GMN strategies, the high sensitivity of the gradients considered above renders them unsuitable for

use in an MR angiography pulse sequence. An approach aimed at reducing this sensitivity involves the use of shortened gradient durations. In the next section, the utility of this approach will be considered.

Gradient Duration

Several investigators have suggested that shortened gradient duration is an effective means of reducing signal loss (1–5). To evaluate the utility of this approach, the effects of shortened gradient duration were studied in the free-jet flow phantom. Images were obtained at a fixed flow rate of 120 cm/sec, with echo asymmetries ranging from 0% to 40%. In the left graph of Figure 9, experimentally observed signal loss areas for the zeroth- through third-order gradients are plotted as a function of echo asymmetry. Clearly, large reductions in signal loss are achieved with asymmetric echoes (ie, shortened gradient durations). As shown in the right graph of Figure 9, similar reductions are predicted for the mean flow component of the signal loss. Consistent with our previous results, the experimental signal loss areas remained large relative to corresponding simulated mean-flow signal loss areas. Notably, the observed signal loss was substantially reduced by shortening of the readout gradient duration, while factors such as TE and the duration of the section-select gradient remained unchanged. Consistent with the observations of Nishimura et al (1), this result indicates that the use of shortened gradient durations, not reductions in TE, accounts for the majority of the observed reduction in signal loss. Furthermore, under the experimental conditions used, the readout gradient is responsible for most of the observed signal loss.

Many features of these data are explained by the relative sensitivity $\Gamma_{k0}(n)$ of the gradients. Because asymmetric echos were formed by linearly scaling the pulse widths of the readout-gradient dephasing lobes, $\Gamma_{k0}(n)$ is a weak function of echo asymmetry (for negligible gradient rise times, $\Gamma_{k0}[n]$ is independent of echo asymmetry because the absolute sensitivity of the gradients will scale with gradient duration [30]). Therefore, to a good approximation, echo asymmetry changes affect only the absolute sensitivity of the gradients, not their relative sensitivity. The relative performance of the first- and higher-order gradients is consistent with this observation, since the area of signal loss observed remained roughly unchanged as the echo asymmetry was varied from 0% to 40%. Only the zeroth-order gradient deviated from this trend, with the size of its experimentally observed signal loss region increasing at a rate greater than those of the other gradients. This effect may be attributed to the sensitivity of the zeroth-order gradient to first-order motions, since the other gradients exhibit zero sensitivity to first-order motions. Higher-order motions are not involved in this effect, since the zeroth-order gradient has a relatively low sensitivity to these motions.

On the basis of these results, it is clear that gradient sensitivity to motions of all orders must be minimized if signal loss induced by disturbed flow is to be reduced. For this criterion to be fulfilled, it is advantageous to use the shortest gradient durations possible (ie, the zeroth-order gradient). However, there are advantages to be gained through first-order GMN. As we have shown, the sensitivity of the zeroth-order gradient to first-order motions causes it to be susceptible to large increases in signal loss when either echo asymmetry or flow rate is changed. In contrast, the first-order gradient is less susceptible to large changes, owing to the nulling of first-order motions. Since, generally, the nature of a flow field is unknown, this suggests that first-order GMN will be a more robust means of flow compensation than zeroth-order GMN.

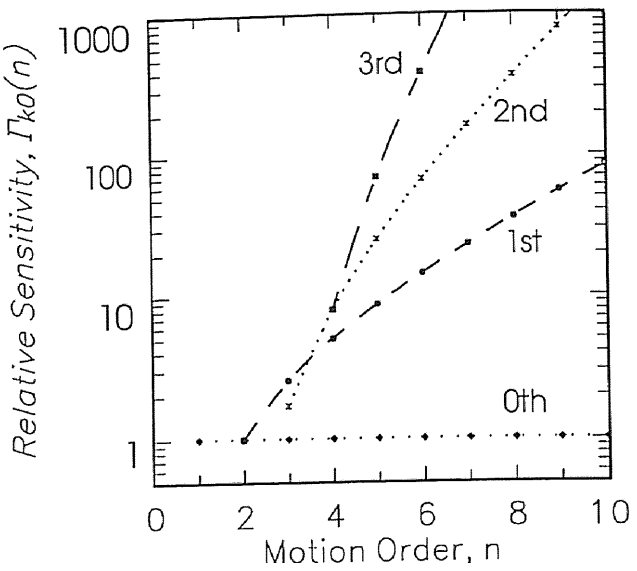

Figure 8. Relative sensitivity of the zeroth- through third-order gradients plotted versus motion order.

The increased sensitivity of the higher-order gradients is a consequence of their relatively long durations, as determined by gradient-power and image-encoding constraints. If these constraints were relaxed, it might be possible to construct higher-order gradients with reduced overall duration. Since this would act to minimize their increased sensitivity to higher-order motions, use of these gradients might prove to be a more effective means of flow compensation. However, with current clinical imaging hardware, this is not practical.

• DISCUSSION

In this report, we have shown that fluctuating fluid motions induced most of the signal loss in our model flow system. In contrast, mean fluid motions induce substantial signal loss over a relatively small region. These results are consistent with the expected distribution of flow velocity within the flow phantom. In general, large velocity gradients will be localized about the flow constriction, while the intensity (ie, root-mean-square magnitude) of the velocity fluctuations will generally be greatest near and distal to the largest spatial gradients in the mean velocity. Similar flow features will exist in circularly symmetric and more complex stenosis geometries (8). Hence, our results suggest that in stenotic flow, two distinct regions in which signal loss occurs might be envisioned: near the constriction itself, where mean fluid motions induce signal loss, and distal to the constriction, where

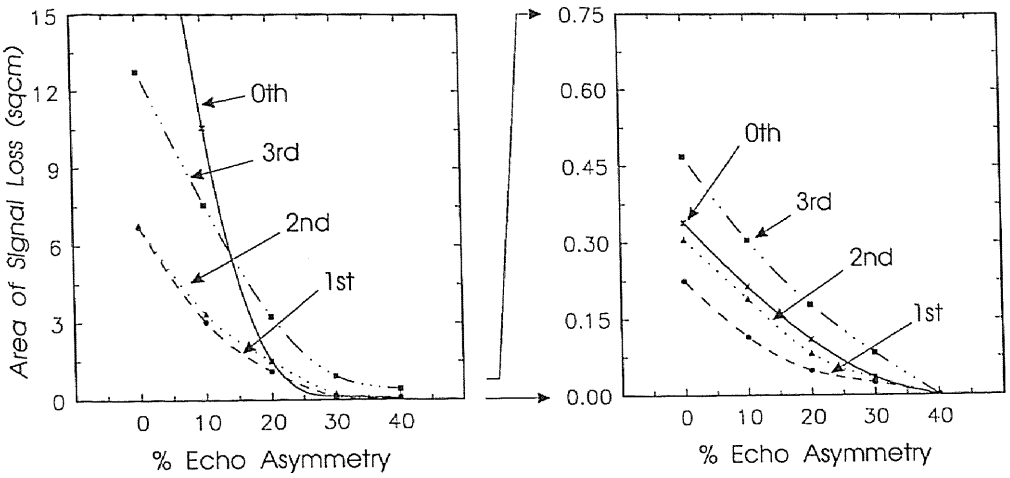

Figure 9. Experimental (left graph) and simulated mean-flow (right graph) signal loss areas plotted versus echo asymmetry for zeroth- through third-order GMN. Error bars have been removed for clarity.

fluctuating motions induce a relatively large region of signal loss.

In this study, use of GMN above first order was found to be an ineffective means of reducing signal loss. While consistent with the observations of several investigators (1,2,4,5), this result contradicts claims made in the literature (3,30,31), which suggest that higher-order GMN is an effective means of reducing signal loss. In one of these reports (30), a comparison is made between gradients of similar duration. In the context of MR angiography, such a comparison is unrealistic because the motion sensitivity of a gradient is a strong function of gradient duration. As considered in the present study, a more appropriate comparison is between gradient waveforms whose durations have been kept as short as possible. Similarly, while the results of Ruggieri et al (3) and Guo et al (31) suggest that a short, second-order readout gradient is the optimal means of flow compensation, it is unclear from these reports whether the duration of the first-order gradient used in these comparisons was minimized. Nevertheless, it is clear that the use of short gradient durations is an effective means of reducing signal loss. However, our results indicate that there are advantages to be gained with first-order GMN because it provides the most robust alternative for minimizing signal loss. These data suggest that MR angiography is best performed with short-duration, first-order readout gradients. ●

Acknowledgments: The helpful suggestions of Michael Bronskill, PhD, and Michael Wood, PhD, are greatly appreciated.

References

1. Nishimura DG, Macovski A, Jackson JI, Hu RS, Stevick CA, Axel L. Magnetic resonance by selective inversion recovery using a compact gradient echo sequence. Magn Reson Med 1988; 8:96–103.
2. Keller PJ, Drayer BP, Fram EK, Williams KD, Dumoulin CL, Souza SP. MR angiography with two-dimensional acquisition and three-dimensional display. Radiology 1989; 173:527–532.
3. Ruggieri PM, Laub GA, Masaryk TJ, Modic MT. Intracranial circulation: pulse-sequence considerations in three-dimensional (volume) MR angiography. Radiology 1989; 171:785–791.
4. Schmalbrock P, Yuan C, Chakeres DW, Kohli J, Pelc NJ. Volume MR angiography: methods to achieve very short echo times. Radiology 1990; 175:861–865.
5. Lewin JS, Laub G. Intracranial MR angiography: a direct comparison of three time-of-flight techniques. AJNR 1991; 12:1133–1139.
6. Dumoulin CL, Souza SP, Walker MF, Wagle W. Three-dimensional phase contrast angiography. Magn Reson Med 1989; 9:139–149.
7. Milnor WR. Hemodynamics. 2nd ed. Baltimore: Williams & Wilkins, 1989; 34–41.
8. Cassanova RA, Giddens DP. Disorder distal to modeled stenoses in steady and pulsatile flows. J Biomech 1978; 11:441–453.
9. Bradley WG, Waluch V, Lai K, Fernandez EJ, Spalter C. The appearance of rapidly flowing blood on magnetic resonance images. AJR 1984; 143:1167–1174.
10. Nishimura DG, Macovski A, Pauly JM. Magnetic resonance angiography. IEEE Trans Med Imaging 1986; MI-5: 140–151.
11. Evans AJ, Russell BA, Blinder A, et al. Effects of turbulence on signal intensity in gradient echo images. Invest Radiol 1988; 23:512–518.
12. Xiang QS, Nalcioglu O. A formalism for generating multiparametric encoding gradients in NMR tomography. IEEE Trans Med Imaging 1987; MI-6:14–20.
13. Pattany PM, Chiu LC, Lipcamon JD, et al. Motion artifact suppression technique (MAST) for magnetic resonance imaging. J Comput Assist Tomogr 1987; 11:369–377.
14. Haacke EM, Lenz GW. Improving MR image quality in the presence of motion using rephasing gradients. AJR 1987; 148:1251–1258.
15. Fukuda K, Hirai A. A pulsed NMR study on the flow of fluid. J Phys Soc Jpn 1979; 47:1999–2006.
16. Deville G, Landesman A. Expériences d'échos de spins dans un liquide en écoulement. J Phys 1971; 32:67–72.
17. Kawabe Y, Fukuda K, Hirai A. A note on the signal intensity of the second spin echo in CPMG sequence of turbulent flows. J Phys Soc Jpn 1983; 52:2308–2311.
18. Fukuda K, Inouye A, Kawabe Y, Hirai A. Transition from laminar to turbulent flow of water in a pipe measured by a pulsed NMR method. J Phys Soc Jpn 1985; 54:4555–4560.
19. Nalcioglu O, Moran PR. Application of MRI in fluid mechanics of turbulent flow (abstr). Magn Reson Imaging 1987; 5:52.
20. Gao JH, Gore JC. Study of turbulent flow effects in MR imaging (abstr). JMRI 1991; 1:236.
21. Stepišnik J. Measuring and imaging of flow by NMR. Prog NMR Spectroscopy 1985; 17:187–209.
22. Nalcioglu O, Moran PR. Effect of turbulent flow on NMR images (abstr). Magn Reson Imaging 1987; 5:418.

23. Kuethe DO. Measuring distributions of diffusivity in turbulent fluids with magnetic resonance imaging. Phys Rev A 1989; 40:4542–4551.
24. McComb WD. The physics of turbulence. Oxford, England: Clarendon, 1990; 7.
25. Mitchell MD, Kundel HL, Axel L, Joseph PM. Agarose as a tissue equivalent phantom material for NMR imaging. Magn Reson Imaging 1986; 4:263–266.
26. Press WH, Flannery BP, Teukolsky SA, Vetterling WT. Numerical recipes in C. Cambridge, England: Cambridge University Press, 1988; 109–110.
27. Schlichting H. Boundary layer theory. New York: McGraw-Hill, 1979; 745–747.
28. Wood ML, Henkelman RM. MR image artifacts from periodic motion. Med Phys 1985; 12:143–151.
29. Wedeen VJ, Wendt RE, Jerosch-Herold M. Motion phase artifacts in Fourier transform MRI. Magn Reson Med 1989; 11:114–120.
30. Duerk JL, Simonetti OP, Hurst GC. Modified gradients for motion suppression: variable echo time and variable bandwidth. Magn Reson Imaging 1990; 8:141–151.
31. Guo Q, Kashmar G, Nalcioglu O. NMR angiography with enhanced quasi-half-echo scanning. Magn Reson Imaging 1991; 9:129–139.